Mon. Not. R. Astron. Soc. **000**, 000–000 (0000) Printed 8 August 2005 (MN LaTeX style file v2.2)

The dependence of the initial mass function on metallicity, and the opacity limit for fragmentation

Matthew R. Bate*
[1]*School of Physics, University of Exeter, Stocker Road, Exeter EX4 4QL*

Accepted for publication in MNRAS

ABSTRACT

We investigate the dependence of stellar properties on the opacity limit for fragmentation which is set by the metallicity of a molecular cloud. We compare the results from two large-scale hydrodynamical simulations of star cluster formation that resolve the fragmentation process down to the opacity limit, the first of which was reported by Bate, Bonnell & Bromm. The initial conditions of the two calculations are identical, but in the new simulation the onset of the opacity limit occurs at a lower gas density, and this is expected to increase the minimum mass of a brown dwarf by a factor of three (to $\approx$ 9 Jupiter masses).

We find that the lowest mass object is a factor of three higher in the low-metallicity calculation, as expected. However, apart from this shift of the low-mass cut-off, the initial mass functions (IMFs) produced by the two calculations are indistinguishable. In particular, the median (characteristic) mass is unchanged. These results add support to the accretion-ejection model proposed by Bate & Bonnell for the origin of the IMF, which predicts that the characteristic mass should vary in proportion to the mean thermal Jeans mass in the cloud. They also indicate that the form of the IMF above the low-mass cut-off should not display a strong metallicity dependence, assuming that the cooling is dominated by dust and that the overall mean thermal Jeans mass of a molecular cloud does not depend on its metallicity. However, if the mean thermal Jeans mass of a molecular cloud is set by the thermal behaviour of gas during the *formation of the cloud*, this should lead to an *indirect* dependence of the characteristic mass of the IMF on metallicity because of the link between the characteristic mass and the mean thermal Jeans mass of the cloud.

Key words: accretion, accretion discs – binaries: general – hydrodynamics – metallicity – stars: formation – stars: low-mass, brown dwarfs – stars: luminosity function, mass function.

1 INTRODUCTION

Understanding the origin of the stellar initial mass function (IMF) is one of the fundamental goals of a complete theory of star formation. One of the primary characteristics of the IMF is its characteristic mass. Why is the typical stellar mass a few tenths of a solar mass? One possibility is that the characteristic mass originates from the typical Jeans mass in the progenitor molecular cloud. This may be the thermal Jeans mass (Larson 1992, 2005), a magnetic critical mass, or a turbulent Jeans mass (Silk 1995). A Jeans mass origin for the characteristic stellar mass has been backed up by early hydrodynamical calculations of the fragmentation of clumpy and turbulent molecular clouds in which it was found that the mean mass of the protostars was similar to the mean initial Jeans mass in the cloud (Klessen, Burkert & Bate 1998; Klessen & Burkert 2000, 2001; Klessen 2001). Another possibility is that the characteristic mass is due to the opacity limit for fragmentation, which sets a lower limit to the mass of a 'star' and all other objects accrete to final masses greater than this minimum mass (Hoyle 1953).

Over the past few years, we have performed large-scale hydrodynamical calculations of the collapse and fragmentation of turbulent molecular clouds to investigate the origins of stellar properties. The calculations resolve down to the opacity limit for fragmentation and, thus, capture the formation of all stars and brown dwarfs. Results from the first two calculations have already been published (Bate, Bonnell & Bromm 2002a, 2002b, 2003; Bate & Bonnell 2005). These calculations followed the fragmentation of turbulent 50-$M_\odot$ clouds with mean initial thermal Jeans masses of 1 $M_\odot$and 1/3 $M_\odot$. Here, we report the results of a third calculation, identical to the first, except that the opacity limit for fragmentation set in at a gas density nine times lower, resulting in a minimum mass that was three times greater than in the first calculation ($\approx$ 9 Jupiter masses instead of 3 Jupiter masses for the first two calculations).

Together, these three calculations enable us to examine the dependence of stellar properties on the mean thermal Jeans mass and the opacity limit for fragmentation, at last answering the question of which mass scale determines the characteristic mass of the IMF.

* E-mail: mbate@astro.ex.ac.uk

We find that the opacity limit for fragmentation does not significantly influence the characteristic mass or the form of the IMF, except that it sets the value of the low-mass cut-off.

The paper is structured as follows. Section 2 briefly describes the numerical method and the initial conditions for the calculations. The results are discussed in Section 3. In Section 4, we discuss the implications of the results for the origin of the IMF. Our conclusions are given in Section 5.

2 COMPUTATIONAL METHOD

The calculations presented here were performed using a three-dimensional, smoothed particle hydrodynamics (SPH) code. The SPH code is based on a version originally developed by Benz (Benz 1990; Benz et al. 1990). The smoothing lengths of particles are variable in time and space, subject to the constraint that the number of neighbours for each particle must remain approximately constant at $N_{\rm neigh} = 50$. The SPH equations are integrated using a second-order Runge-Kutta-Fehlberg integrator with individual time steps for each particle (Bate, Bonnell, & Price 1995). Gravitational forces between particles and a particle's nearest neighbours are calculated using a binary tree. We use the standard form of artificial viscosity (Monaghan & Gingold 1983; Monaghan 1992) with strength parameters $\alpha_{\rm v} = 1$ and $\beta_{\rm v} = 2$. Further details can be found in Bate et al. (1995). The code has been parallelised by M. Bate using OpenMP.

2.1 Equation of state

To model the thermal behaviour of the gas without performing radiative transfer, we use a barotropic equation of state for the thermal pressure of the gas $p = K\rho^{\eta}$, where K is a measure of the entropy of the gas. The value of the effective polytropic exponent η, varies with density as

$$\eta = \begin{cases} 1, & \rho \le \rho_{\rm crit}, \\ 7/5, & \rho > \rho_{\rm crit}. \end{cases} \tag{1}$$

We take the mean molecular weight of the gas to be $\mu = 2.46$. The value of K is defined such that when the gas is isothermal $K = c_{\rm s}^2$, with the sound speed $c_{\rm s} = 1.84 \times 10^4$ cm s^{-1} at 10 K, and the pressure is continuous when the value of η changes.

In this paper, three different calculations are discussed. The value of the critical density above which the gas becomes non-isothermal is set to $\rho_{\rm crit} = 10^{-13}$ g cm^{-3} in the first two calculations. This equation of state has been chosen to match closely the relationship between temperature and density during the spherically-symmetric collapse of molecular cloud cores with solar metallicity as calculated with frequency-dependent radiative transfer (see Bate et al. 2003 for further details). In the third calculation (which is the main focus of this paper), we set the critical density to be a factor of nine lower at $\rho_{\rm crit} = 1.1 \times 10^{-14}$ g cm^{-3}. This is meant to mimic the thermal behaviour of molecular gas that has a lower metallicity.

The heating of the molecular gas that begins at the critical density inhibits fragmentation at higher densities. This effect is known as the opacity limit for fragmentation (Low & Lynden-Bell 1976; Rees 1976; Silk 1977a, 1977b). It results in the formation of distinct pressure-supported fragments within collapsing gas because the temperature increases quickly enough with density that the Jeans mass increases, and the high density region that was collapsing becomes Jeans stable. It stops collapsing and can only contract as it accretes mass. The value of the initial mass of a fragment presumably also gives the minimum mass for a brown dwarf, since any subsequent accretion will only increase a fragment's mass. This minimum mass depends on the value of the critical density and is approximately equal to the Jeans mass at that density and temperature. Since the critical density is a factor of nine lower in the third calculation, the minimum mass is expected to be a factor of three higher than in the other two calculations. The lowest mass object produced by Calculations 1 and 2 was $\approx$ 3 Jupiter masses (M$_{\rm J}$). Thus, the lowest mass object in the third calculation is expected to be ≈ 9 M$_{\rm J}$.

Physically, the heating of the gas that results in a minimum mass is due to the inability of the gas to radiate away energy as quickly as energy is being deposited into it during the collapse (Masunaga & Inutsuka 1999). The gas cooling depends on its metallicity, Z, and Low & Lynden-Bell (1976) found that the minimum mass scales weakly with metallicity as $Z^{-1/7}$. They assumed that the conditions in the minimum mass fragment were given by a balance between radiative cooling and compressional work done on the collapsing gas as the fragment became optically thick. Since radiative cooling is proportional to κT^4 where κ is the opacity and T is the temperature, then a lower metallicity (and hence a lower opacity) results in the fragment having a greater temperature. By balancing the radiative cooling and compressional heating when the fragment becomes optically thick, Low & Lynden-Bell show that the fragment's temperature scales as $T \propto \kappa^{-4/7}$. However, for the fragment to be optically thick and marginally Jeans unstable requires $\kappa\rho\lambda_{\rm J}/2 = 1$, where the Jeans unstable wavelength $\lambda_{\rm J} = 2\pi\sqrt{R_{\rm g}T/(4\pi G\rho\mu)}$, $R_{\rm g}$ is the gas constant, G is the gravitational constant, and μ is the mean molecular weight (i.e., $\kappa^2 T/\rho$ = a constant). Therefore, using the above scaling of temperature with opacity, the density of the fragment $\rho \propto \kappa^{-10/7}$. Thus, both the temperature and density of the fragment are higher for lower metallicity gas. The weak dependence of the fragment's mass on metallicity is due to a near cancellation of the two scalings of temperature and density on opacity since the Jeans mass is proportional to $T^{3/2}\rho^{-1/2} \propto \kappa^{-1/7}$. Note that Masunaga & Inutsuka (1999) question Low & Lynden-Bell's assumption that the fragment is always optically thick when cooling balances heating. However, if the minimum mass does scale as $Z^{-1/7}$, then Calculation 3 corresponds to a metallicity of around 5×10^{-4} of the solar value (i.e., $\log(Z/Z_\odot) = -3.3$).

2.2 Sink particles

As the pressure-supported fragments accrete, their central density increases, and it becomes computationally impractical to follow their internal evolution because of the short dynamical timescales involved. Therefore, when the central density of a pressure-supported fragment exceeds $\rho_{\rm s} = 100\rho_{\rm crit}$, we insert a sink particle into the calculation (Bate et al. 1995).

In all the calculations discussed in this paper, a sink particle is formed by replacing the SPH gas particles contained within $r_{\rm acc} = 5$ AU of the densest gas particle in a pressure-supported fragment by a point mass with the same mass and momentum. Any gas that later falls within this radius is accreted by the point mass if it is bound and its specific angular momentum is less than that required to form a circular orbit at radius $r_{\rm acc}$ from the sink particle. Thus, gaseous discs around sink particles can only be resolved if they have radii $\gtrsim 10$ AU. Sink particles interact with the gas only via gravity and accretion.

Since all sink particles are created from pressure-supported fragments, their initial masses are several M$_{\rm J}$, as given by the opac-

Calculation	Initial Gas Mass $M_\odot$	Initial Radius pc	Jeans Mass $M_\odot$	Mach No.	Heating Density g cm^{-3}	No. Stars Formed	No. Brown Dwarfs	Mass of Stars & Brown Dwarfs $M_\odot$	Mean Mass $M_\odot$	Median Mass $M_\odot$
1	50.0	0.188	1	6.4	10^{-13}	≥23	≤27	5.89	0.1178	0.070
2	50.0	0.090	1/3	9.2	10^{-13}	≥19	≤60	7.92	0.1003	0.023
3	50.0	0.188	1	6.4	1.1×10^{-14}	≥16	≤18	6.88	0.2024	0.054

Table 1. The initial conditions for calculations 1 (BBB2003), 2 (BB2005) and 3 (this paper) and the statistical properties of the stars and brown dwarfs formed. The initial conditions for Calculation 3 were identical to those of Calculation 1. The only difference was the density at which gas heating began which was a factor of 9 lower in Calculation 3 than in Calculation 1. Calculation 2 differed from Calculation 1 in that the initial cloud had a smaller radius making the mean thermal Jeans mass a factor of 3 lower. In each case, the initial turbulent velocity fields where identical and were scaled so that for each cloud the initial kinetic energy equalled the magnitude of the gravitational potential energy. All calculations were run for 1.40 initial cloud free-fall times. Brown dwarfs are defined as having final masses less than 0.075 $M_\odot$. The numbers of stars (brown dwarfs) are lower (upper) limits because some of the brown dwarfs were still accreting when the calculations were stopped.

ity limit for fragmentation. Subsequently, they may accrete large amounts of material to become higher-mass brown dwarfs ($\lesssim 75$ M_J) or stars ($\gtrsim 75$ M_J), but *all* the stars and brown dwarfs begin as these low-mass pressure-supported fragments.

The gravitational acceleration between two sink particles is Newtonian for $r \geq 4$ AU, but is softened within this radius using spline softening (Benz 1990). The maximum acceleration occurs at a distance of ≈ 1 AU; therefore, this is the minimum separation that a binary can have even if, in reality, the binary's orbit would have been hardened. Sink particles are not permitted to merge in this calculation.

The benefits and potential problems associated with introducing sink particles are discussed in more detail by Bate et al. (2003).

2.3 Initial conditions

We report on the results from three calculations. Together, these three calculations test the dependence of the statistical properties of star formation (such as the IMF) on the mean thermal Jeans mass in the initial clouds and the opacity limit for fragmentation (or metallicity of the gas). Results from Calculation 1 were presented in Bate et al. (2002a, 2002b, 2003), while Bate & Bonnell (2005) compared the results from Calculations 1 and 2. Henceforth, we will refer to the latter two of these papers as BBB2003 and BB2005.

The initial conditions and results from all three calculations are summarised in Table 1. Each calculation models star formation in a 50-$M_\odot$ molecular cloud which is set up as a uniform-density spherical cloud with an imposed supersonic 'turbulent' velocity field that is allowed to decay as the calculation evolves (see BBB2003 and BB2005 for further details).

Calculations 1 and 3 were identical except for the value of $\rho_{\rm crit}$ at which the gas departed from isothermality. In fact, the initial stages of Calculation 3 were not even calculated – Calculation 3 was simply started from the last dump file that was made before Calculation 1 reached 10^{-14} g cm^{-3}.

The differences between the initial conditions for Calculations 1 and 2 were discussed in detail by BB2005. Essentially the clouds were identical except for radii of the initial clouds which differed such that the molecular cloud in Calculation 2 was nine times denser than that of Calculation 1 and, hence, the initial mean thermal Jeans mass was three times lower in Calculation 2 (see Table 1). Another slight difference was that, in order that the kinetic energy in the turbulence balanced the gravitational potential energy of each of the clouds, the initial Mach number of the 'turbulence' in Calculation 2 was slightly higher than that in Calculations 1 and 3 (see Table 1).

Finally, we note that the free-fall times of the clouds in Calculations 1 and 3 were $t_{\rm ff} = 6.0 \times 10^{12}$ s or 1.90×10^5 years, while in Calculation 2 $t_{\rm ff} = 2.0 \times 10^{12}$ s or 6.34×10^4 years.

2.4 Resolution

The local Jeans mass must be resolved throughout the calculations to model fragmentation correctly (Bate & Burkert 1997; Truelove et al. 1997; Whitworth 1998; Boss et al. 2000; Nelson 2005). This requires $\gtrsim 1.5 N_{\rm neigh}$ SPH particles per Jeans mass; $N_{\rm neigh}$ is insufficient (Bate et al. 2003). The minimum Jeans mass in Calculations 1 and 2 occurs at the maximum density during the isothermal phase of the collapse, $\rho_{\rm crit} = 10^{-13}$ g cm^{-3}, and is ≈ 0.0011 $M_\odot$ (1.1 M_J). Thus, we used 3.5×10^6 particles to model the 50-$M_\odot$ clouds. For Calculation 3, the minimum Jeans mass is a factor of 3 greater because of the decrease in the value of $\rho_{\rm crit}$, but because the calculation is restarted from an early dump file of Calculation 1 it still uses 3.5×10^6 particles. Thus, in Calculation 3, a local Jeans mass is always resolved by at least $3 \times 1.1 \times 1.5 N_{\rm neigh} \approx 250$ SPH particles

The calculations required approximately 95000, 50000, and 75000 CPU hours, respectively, on the SGI Origin 3800 of the United Kingdom Astrophysical Fluids Facility (UKAFF).

3 COMPARISON OF RESULTS

The results of Calculations 1 and 2 were published in BBB2003 and BB2005. In these papers, the global evolution of the clouds, the star formation efficiencies and timescales, the forms of the stellar initial mass functions, the formation mechanisms of brown dwarfs and close binaries, the multiplicities and velocity dispersions of the objects, and the properties of their circumstellar discs we examined in detail. In this paper, we present the results of Calculation 3 in an identical manner to the past calculations through the figures and tables, but in the text we concentrate on how the results *differ* from the other two calculations. In particular, we concentrate on understanding the roles of the opacity limit for fragmentation (i.e., metallicity) and the mean thermal Jeans mass in the progenitor molecular cloud in determining the statistical properties of the stars and brown dwarfs.

3.1 Evolution of the clouds

As stated in Section 2.3, the initial conditions and evolution of Calculations 1 and 3 are identical up to the point that the gas first exceeds the density at which it departs from isothermality, $\rho_{\rm crit}$,

Core	Initial Gas Mass $M_\odot$	Initial Size pc	Final Gas Mass $M_\odot$	No. Stars Formed	No. Brown Dwarfs Formed	Mass of Stars and Brown Dwarfs $M_\odot$	Star Formation Efficiency %
1	3.04 (0.79)	$0.06 \times 0.04 \times 0.03$	2.83 (1.21)	≥10	≤17	6.00	68 (83)
2	0.89 (0.22)	$(0.02 \times 0.01 \times 0.01)$	1.06 (0.30)	3	0	0.41	29 (58)
3	1.12 (0.33)	$(0.02 \times 0.01 \times 0.01)$	1.09 (0.30)	3	1	0.46	30 (61)
Cloud	50.0	$0.38 \times 0.38 \times 0.38$	43.1	≥16	≤18	6.88	14

Table 2. The properties of the three dense cores that form during Calculation 3 and those of the cloud as a whole. The gas masses and sizes of the cores are calculated from gas with $n(\mathrm{H_2}) > 1 \times 10^6$ cm^{-3} and $n(\mathrm{H_2}) > 1 \times 10^7$ cm^{-3} (the latter values are given in parentheses). The initial gas mass is calculated just before star formation begins in that core (i.e. different times for each core). Brown dwarfs have final masses less than 0.075 $M_\odot$. The star formation efficiency is taken to be the total mass of the stars and brown dwarfs that formed in a core divided by the sum of this mass and the mass in gas in that core at the end of the calculation. As with Calculation 1, the star formation efficiency is high locally, but low globally. The numbers of stars (brown dwarfs) are lower (upper) limits because fourteen of the brown dwarfs were still accreting when the calculation was stopped.

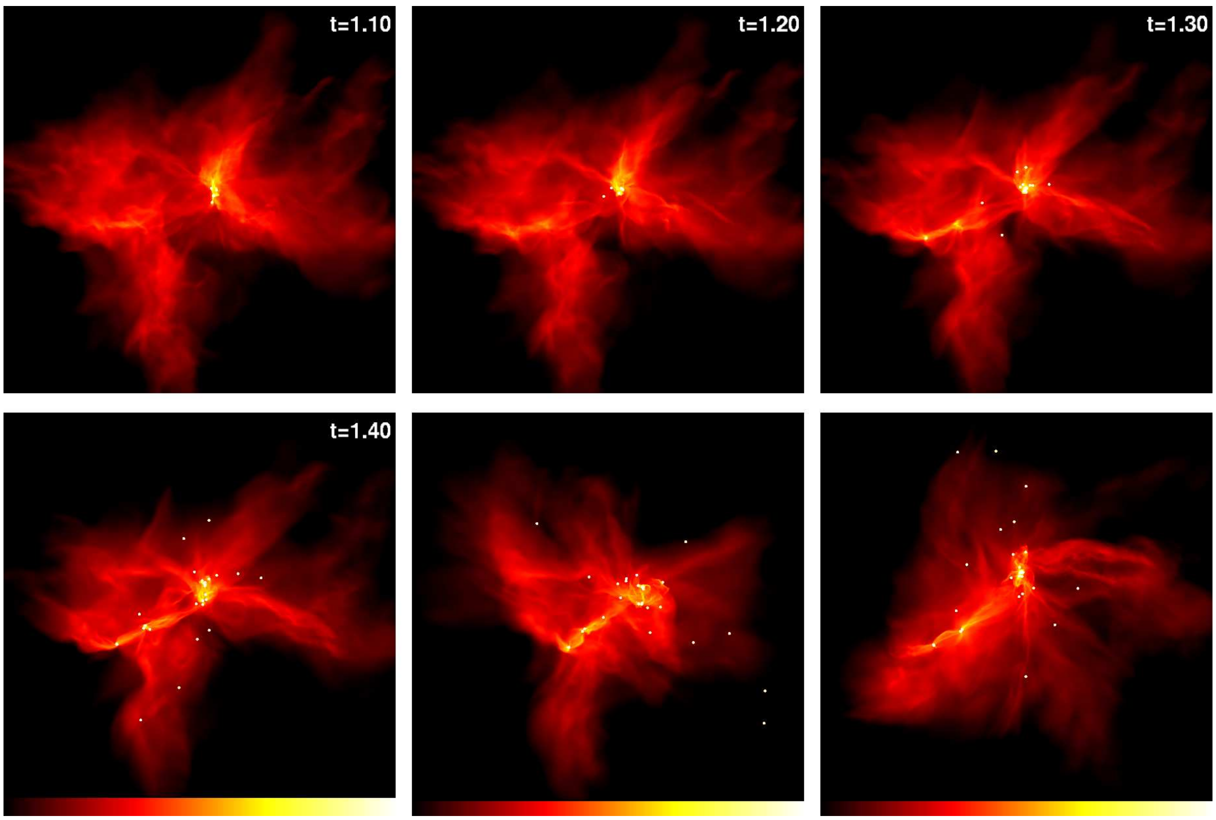

Figure 1. The global evolution of the cloud during Calculation 3 for comparison with Figure 2 of BBB2003 for Calculation 1. Images are only shown at times $t = 1.10 - 1.40 t_{\rm ff}$ because Calculation 3 was started from the $t = 1.028 t_{\rm ff}$ dump file of Calculation 1, while the molecular gas was still isothermal. The evolution prior to this time can be seen in Figure 2 of BBB2003. The last three panels all show the cloud at the end of the simulation ($t = 1.40 t_{\rm ff}$), but they are from three different angles (along the x, y, and z-axes). As in Calculation 1, by the end of Calculation 3, three dense cores have formed stars (one main dense core, and two smaller cores visible at the left-hand side of the bottom-left panel). Many of the stars and brown dwarfs that formed in the main dense core have been ejected from the cloud through dynamical interactions. Each panel is 0.4 pc (82400 AU) across. Time is given in units of the initial free-fall time of 1.90×10^5 yr. The panels show the logarithm of column density, N, through the cloud, with the scale covering $-1.7 < \log N < 1.5$ with N measured in g cm^{-2}. This column density scale is chosen to allow direct comparison with Calculation 1.

and, thus, Calculation 3 is simply started from a dump file of Calculation 1 that was made at $t = 1.028 t_{\rm ff}$. For a detailed discussion of the earlier evolution of the cloud the reader is referred to BBB2003. Briefly, however, due to the initial velocity dispersion the cloud quickly develops shocks, simultaneously losing kinetic energy and developing overdensities in regions with converging gas flows. When gravity dominates in an overdense region, gravitational collapse occurs and star formation begins.

The clouds modelled in Calculations 1 and 3 each form three dense star-forming cores with essentially identical locations and masses (compare Table 2 with Table 1 of BBB2003 and Figure 1 with Figure 2 of BBB2003). Because of the extra thermal support in Calculation 3, star formation (i.e., the replacing of collapsed gas with sink particles) occurs slightly later in each of the three dense cores than in Calculation 1. The three dense cores begin forming stars at $t = 1.038 t_{\rm ff}$, $t = 1.298 t_{\rm ff}$, and $t = 1.320 t_{\rm ff}$, respectively.

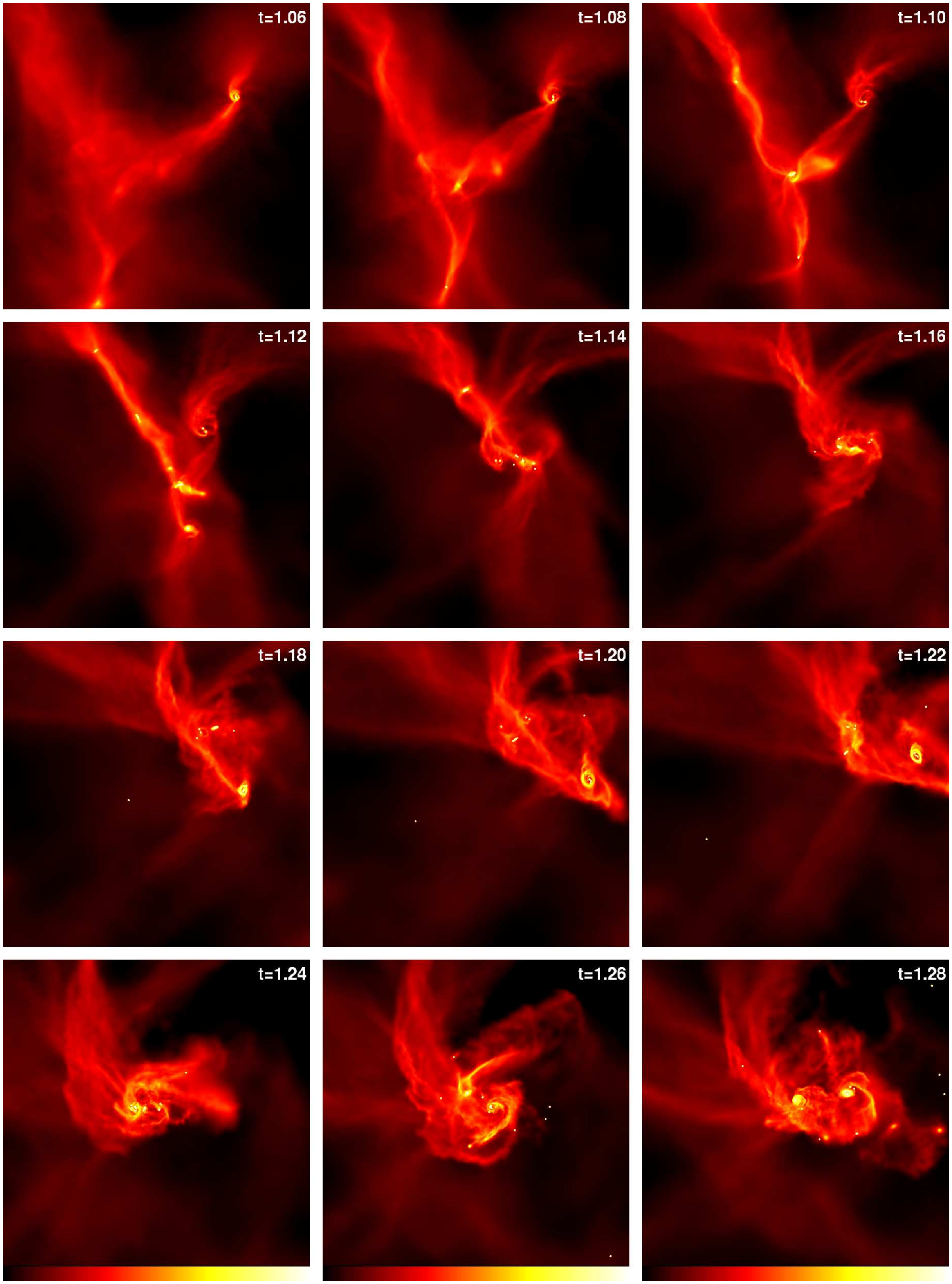

Figure 2. The star formation in the first (main) dense core of Calculation 3. The first objects form a binary at $t = 1.038t_{\rm ff}$. Large gaseous filaments collapse to form single objects and multiple systems. These objects fall together to form a small group. In Calculation 1, the equivalent group quickly dissolved due to dynamical interactions. However, in Calculation 3 only one object is ejected quickly – the rest settle into a wide group of objects. and, simultaneously, there is a quiet period ($t = 1.16 - 1.24t_{\rm ff}$) in the star formation while more gas falls into the core. At $t \approx 1.26$, a new burst of star formation begins in the filamentary gas and in a large disc around a close binary. The sequence is continued in Figure 3. Each panel is 0.025 pc (5150 AU) across. Time is given in units of the initial free-fall time of 1.90×10^5 years. The panels show the logarithm of column density, N, through the cloud, with the scale covering $-0.5 < \log N < 2.5$ with N measured in g cm^{-2}.

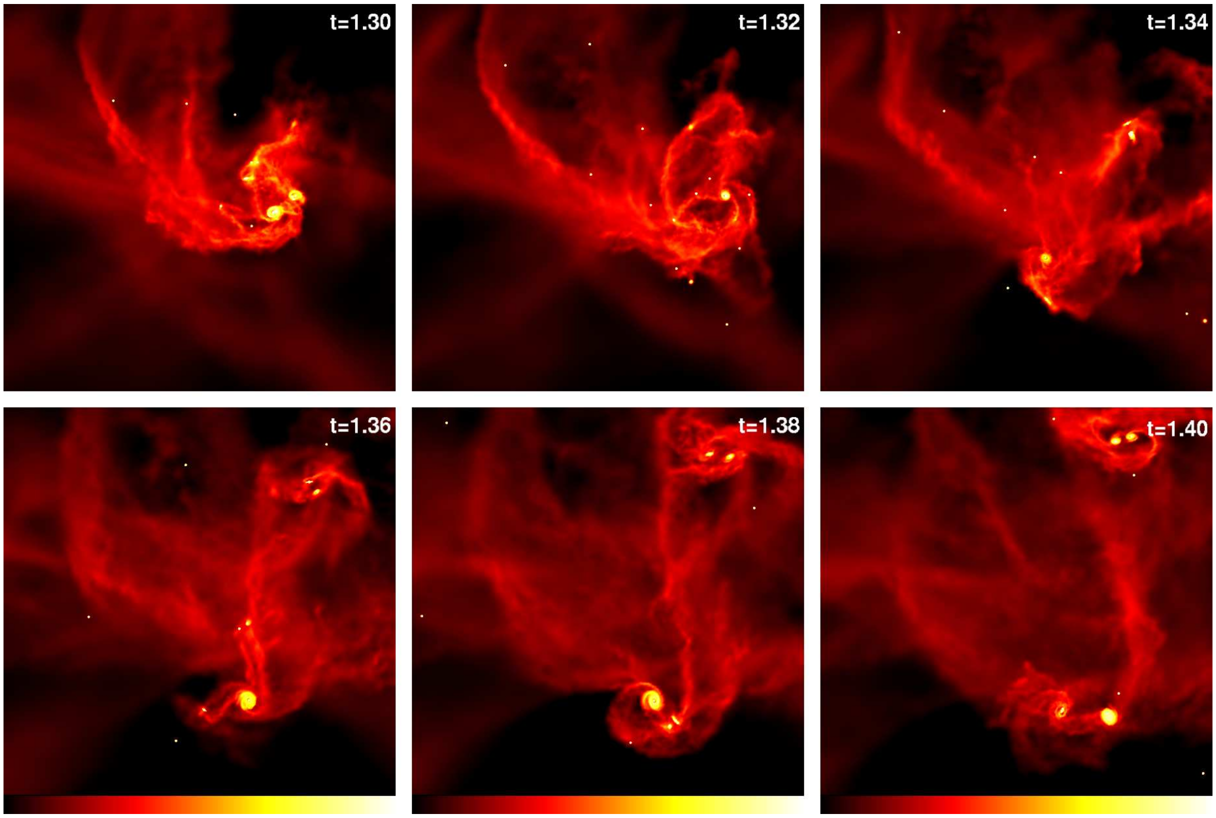

Figure 3. The star formation in the first (main) dense core, continued from Figure 2. The second burst of star formation again produces a small group of objects. This group has essentially dissolved by the time the calculation is stopped. Note the system at the top-right of the lower panels – this sytstem is the 220-AU quadruple system (1,2),(6,8) consisting of two close binaries each surrounded by a circumbinary disc (see also Tables 3 and 4). The system at the bottom-right of the lower panels is the quadruple system (3,(5,22),17) which contains a circumstellar disc around object 3 and a circumbinary disc around the 39-AU binary (5,22). Each panel is 0.025 pc (5150 AU) across. Time is given in units of the initial free-fall time of 1.90×10^5 years. The panels show the logarithm of column density, N, through the cloud, with the scale covering $-0.5 < \log N < 2.5$ with N measured in g cm^{-2}.

In each case, these times are approximately $0.002t_{\rm ff}$ later than the corresponding times in Calculation 1.

All three calculations were stopped at $t = 1.40t_{\rm ff}$ to allow direct comparison of the results. Star formation would continue in each cloud if the calculations were followed further. Calculation 3 produced 16 stars and 16 brown dwarfs. Two additional objects had substellar masses but were still accreting. Both of these formed shortly before the calculation was stopped and, therefore, it is impossible to tell whether or not they would become stars.

3.2 The star-formation process in the dense cores

Snapshots of the process of star formation in Calculation 3 are shown in Figures 2 and 3 for Core 1 and in Figure 4 for Cores 2 and 3. As with the earlier calculations, a true appreciation of how dynamic and chaotic the star-formation process is can only be obtained by studying an animation of the simulation. The reader is encouraged to download an animation comparing Calculations 1 and 3 from http://www.astro.ex.ac.uk/people/mbate/Research/Cluster.

As in Calculation 1, the star formation in the dense cores proceeds via gravitational collapse to produce filamentary structures that fragment (e.g. Bastien 1983; Bastien et al. 1991; Inutsuka & Miyama 1992) to form a combination of single objects and multiple systems (Figures 2, 3 and 4). In Calculation 1, many of the multiple systems result from the fragmentation of massive circumstellar discs (e.g. Bonnell 1994; Bonnell & Bate 1994; Whitworth et al. 1995; Burkert, Bate & Bodenheimer 1997; Hennebelle et al. 2004). This is still the case in Calculation 3 but there is *less* disc fragmentation than in Calculation 1 because the change in the equation of state results in a given disc being hotter and, thus, more stable against fragmentation. A particularly good example of the effect of the change in the equation of state is the evolution of the circumbinary disc that forms around the first two objects (seen in the upper-right of the first four panels in Figure 2 and the equivalent figure of BBB2003). In Calculation 1, this disc fragments to form two stars and a brown dwarf in the interval $t = 1.06-1.08t_{\rm ff}$, but in Calculation 3 the disc does not fragment.

In the most massive core, in both Calculations 1 and 3, the objects fall together into the gravitational potential well of the core to form a small stellar cluster (Figure 2, $t = 1.12-1.14t_{\rm ff}$). At this point, Calculation 3's cluster contains 10 objects (three fewer than in Calculation 1). From this point on, the clusters begin ejecting objects in dynamical interactions. We note that clusters containing more objects appear to be the most efficient at ejecting objects (i.e., they eject the largest number objects in the same fraction of a free-fall time). At $t = 1.26$, Calculation 3 had produced 14 objects but ejected only five of these, whereas Calculation 1 had produced 20 and ejected 15 of these. Calculation 2 had produced 45 objects in Core 1 and ejected ≈ 20 of these at the same time and more than half of the objects shortly afterwards.

Another interesting point that is graphically illustrated by comparing the evolutions of the main dense cores of Calculations 1

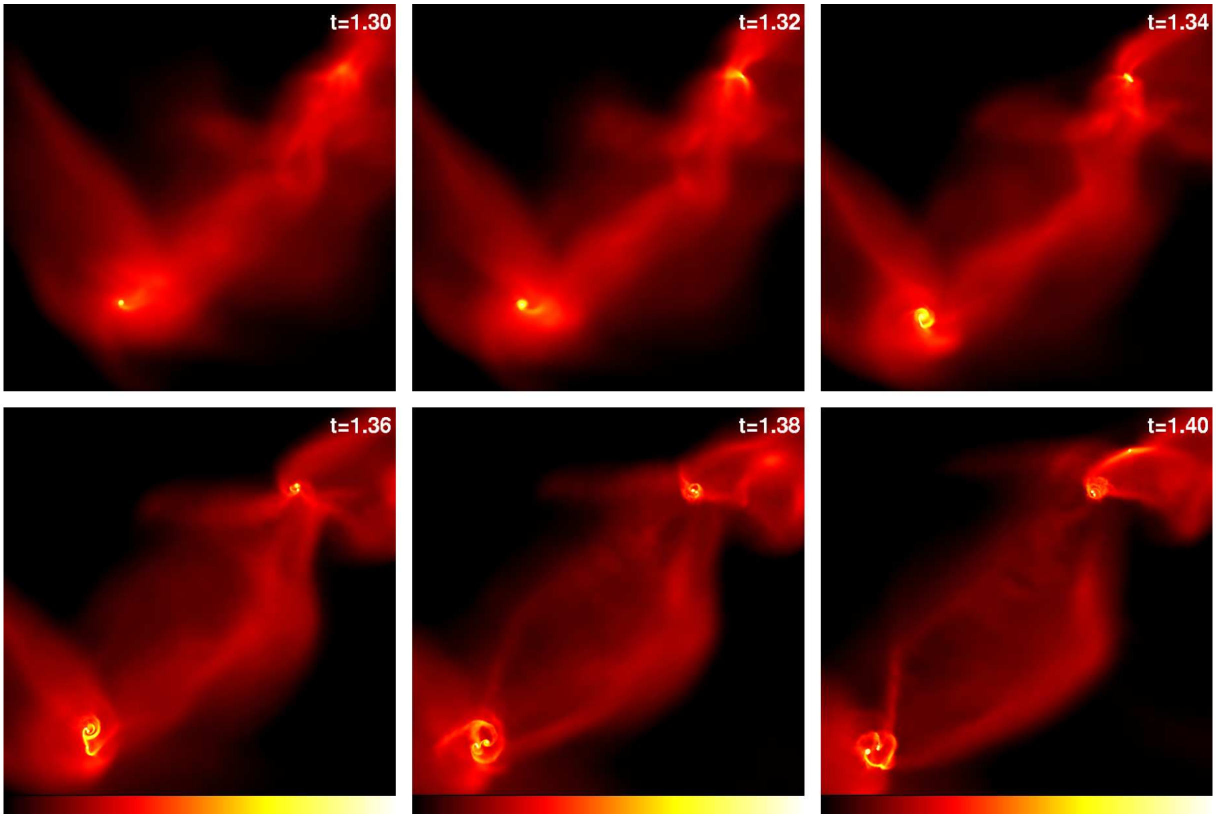

Figure 4. The star formation in the second and third dense cores. The first object in core 2 forms at $t = 1.298t_{\rm ff}$, followed quickly by the first object in core 3 at $t = 1.320t_{\rm ff}$. Both objects are subsequently surrounded by massive circumstellar discs that each fragment to form two triple stellar systems. Just before the a fourth object forms from a filament in core 3 that has the mass of a brown dwarf but is still accreting rapidly when the calculation is stopped. Each panel is 0.025 pc (5150 AU) across. Time is given in units of the initial free-fall time of 1.90×10^5 yr. The panels show the logarithm of column density, N, through the cloud, with the scale covering $-0.5 < \log N < 2.5$ with N measured in g cm^{-2}.

and 3 is the chaotic nature of star formation. Even a small change in the physics (in this case, a slight change to the equation of state) results in parallel evolutions that diverge with time. This can be seen by comparing Figures 2 and 3 with Figures 3 and 4 of BBB2003 (see also the animation). Up until $t = 1.20t_{\rm ff}$, the spatial distributions of star formation within the main dense cores are very similar. However, after this point they become very different, largely due to the break up of a multiple system in Calculation 1 that does not have a counterpart in Calculation 3.

Cores 2 and 3 each produce 3 stars during Calculation 3. Each of these begins with a single star surrounded by a massive disc that fragments to form a triple system. Core 3 also forms a fourth object in a nearby filament, just before the calculation is stopped (see also Figure 6 of BBB2003 for the counterpart of this filament). Again, although disc fragmentation occurs in Calculation 3, it is less prolific than in Calculation 1 in which cores 2 and 3 produced 7 and 5 objects, respectively.

3.3 Star formation timescale and efficiency

The timescale on which star formation occurs is the dynamical one in all three calculations, consistent both with observational and other theoretical arguments (Pringle 1989; Elmegreen 2000a; Hartmann, Ballesteros-Paredes & Bergin 2001), whether or not magnetic fields are present (MacLow et al. 1998;Ostriker et al. 2001; Li et al. 2004). We note that Calculation 3 converts slightly more gas into stars in the same amount of time as Calculation 1 (6.88 versus 5.89 M$_\odot$). Because the calculations are essentially identical on large-scales, this difference probably indicates that accretion is more efficient in clusters containing fewer objects (the gas is less stirred up).

In all calculations, the local star-formation efficiency is high within each of the dense cores (see Table 2 for Calculation 3). This high star-formation efficiency is responsible for the bursts of star formation seen in all three calculations (see Figure 5 for Calculation 3, where there is a burst of star formation in the main dense core from $t = 1.03 - 1.13t_{\rm ff}$, followed by a pause, and a second burst during $t = 1.23 - 1.34t_{\rm ff}$). Gas is rapidly converted into stars in the most massive dense cores and depleted to such an extent that star formation pauses. Fresh gas must fall into the gravitational potential wells of the small clusters before new bursts of star formation can ensue. Although the local star-formation efficiency is high in the dense cores, most of the gas in both calculations is in low-density regions where no star formation occurs. Thus, the overall star formation efficiencies are low (~ 10%) for all calculations. Although none of the calculation have been followed until star formation ceases, in all calculations a large fraction of the gas has drifted off to large distances by the end of the calculations due to the initial velocity dispersion and pressure gradients and is not gravitationally unstable. Thus, the global star formation efficiencies are unlikely to exceed a few tens of percent. Furthermore, although none of our calculations form high-mass stars, feedback from jets, outflows and heating of the gas (none of which are included) would nevertheless be expected to reduce the star formation efficiency further.

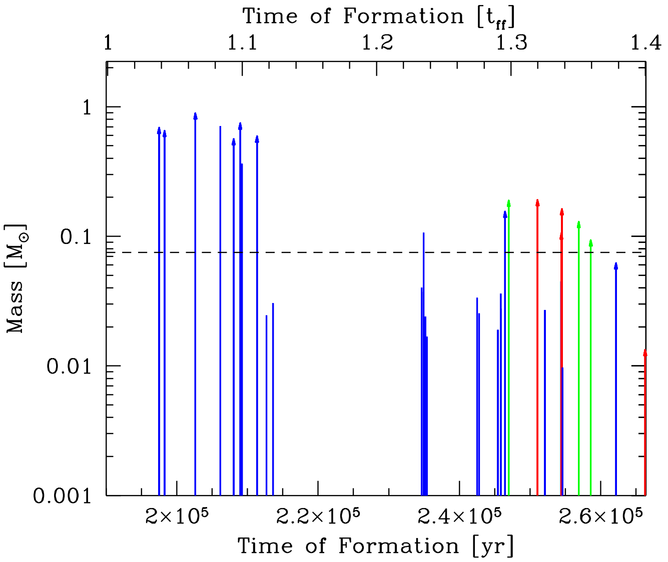

Figure 5. Time of formation and mass of each star and brown dwarf at the end of the calculation. The colour of each line identifies the dense core in which the object formed: first (blue), second (green), or third (red) core. Objects that are still accreting significantly at the end of the calculation a represented with arrows. The horizontal dashed line marks the star/brown dwarf boundary. Time is measured from the beginning of the calculation in terms of the free-fall time of the initial cloud (top) or years (bottom). This figure may be compared with the equivalent figures for Calculations 1 and 2 contained in BBB2003 and BB2005, respectively.

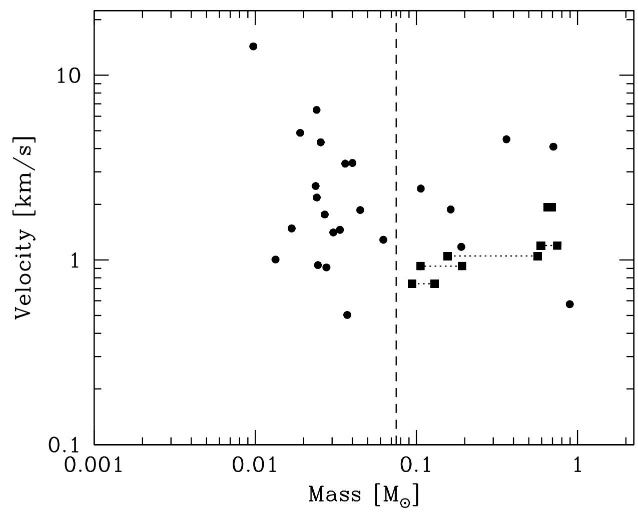

Figure 6. The velocities of each star and brown dwarf relative to the centre-of-mass velocity of the stellar system. For binaries with semi-major axes < 100 AU), the centre-of-mass velocity of the binary is given, and the two stars are connected by dotted lines and plotted as squares rather than circles. The root mean square velocity dispersion for the association (counting each binary once) is 3.7 km/s (3-D) or 2.1 km/s (1-D). As in Calculations 1 and 2, there is no significant dependence of the velocity dispersion on mass. However, up to the end of the new calculation, no binaries were ejected so the velocity dispersion of the binaries is low at only 1.2 km/s (3-D). The vertical dashed line marks the star/brown dwarf boundary.

As discussed in BBB2003, observations show that star formation efficiencies vary widely across star-forming regions. Some parts of star-forming clouds contain no newly formed objects while in other parts, notably clusters and groups, the local efficiency can reach 50% or more. Overall, such a pattern results in low global star formation efficiencies, typically 10-30% (Wilking & Lada 1983; Lada 1992).

3.4 Stellar velocity dispersion

Dynamical interactions between cluster members eject stars and brown dwarfs in all three calculations. In both Calculations 1 and 2, BBB2003 and BB2005 found that the final velocity dispersion of the stars and brown dwarfs is independent both of stellar mass and binarity. While the lack of dependence on mass was reported from past N-body simulations of the breakup of small-N clusters with $N > 3$ (Sterzik & Durisen 1998) and SPH calculations of $N = 5$ clusters embedded in gas (Delgado-Donate, Clarke & Bate 2003), these calculations found that binaries should have a smaller velocity dispersion than single objects due to the recoil velocities of binaries being lower, keeping them within the stellar groups.

The velocities of the stars and brown dwarfs relative to the centre of mass of all the objects are given in Figure 6 for Calculation 3. The rms velocity dispersion is 3.7 km s^{-1} in three dimensions or 2.1 km s^{-1} in one dimension (using the centre-of-mass velocity for binaries closer than 10 AU). This is intermediate between the velocity dispersions of Calculations 1 and 2, which had three-dimensional velocity dispersions of 2.1 and 4.3 km s^{-1}, respectively.

The three-dimensional velocity dispersions of brown dwarfs, stars, and binaries (semi-major axes < 100 AU) are 4.4, 2.8, and 1.2 km s^{-1}, respectively. The difference between the velocity dispersions of the stars and brown dwarfs is not significant since the high brown dwarf velocity dispersion is based purely on a single brown dwarf that was ejected with a velocity of 14 km s^{-1} (removing this object from the sample gives a brown dwarf velocity dispersion of 2.8 km s^{-1}, exactly the same as that of the stars). However, the difference between singles and binaries does appear to be significant. This different result is due to the fact that in Calculations 1 and 2, both single and binary stars were ejected so that their velocity dispersions were indistinguishable whereas, in Calculation 3, all of the binaries are in fact members of triple or high-order systems (see Table 3) and none were ejected before the calculation was stopped resulting in them having a low velocity dispersion. This implies that the lack of dependence of the velocity dispersion on multiplicity that was found in Calculations 1 and 2 is brought about by the fact that most objects in those calculations formed in clusters of $N \gtrsim 20$ objects so that both single objects and multiple systems were ejected. Small multiple systems are efficient at ejecting single objects, but without the larger clusters of objects that formed in Calculations 1 and 2 it is difficult to eject a multiple system. This matches well with the results of Delgado-Donate et al. (2004) who performed simulations of star formation in small turbulent clouds and found while the velocity dispersions of singles and binaries were indistinguishable, higher-order multiples had significantly lower velocity dispersions. The implications for observed star-forming regions are clear. In low-density star-forming regions such as Taurus and Chameleon that form only very small groups of stars, multiple systems may have a lower velocity dispersion than single objects, whereas in richer star-forming regions such as ρ Ophiuchus and Orion there may be no distinction between the velocity dispersions of single and multiple systems. Note also

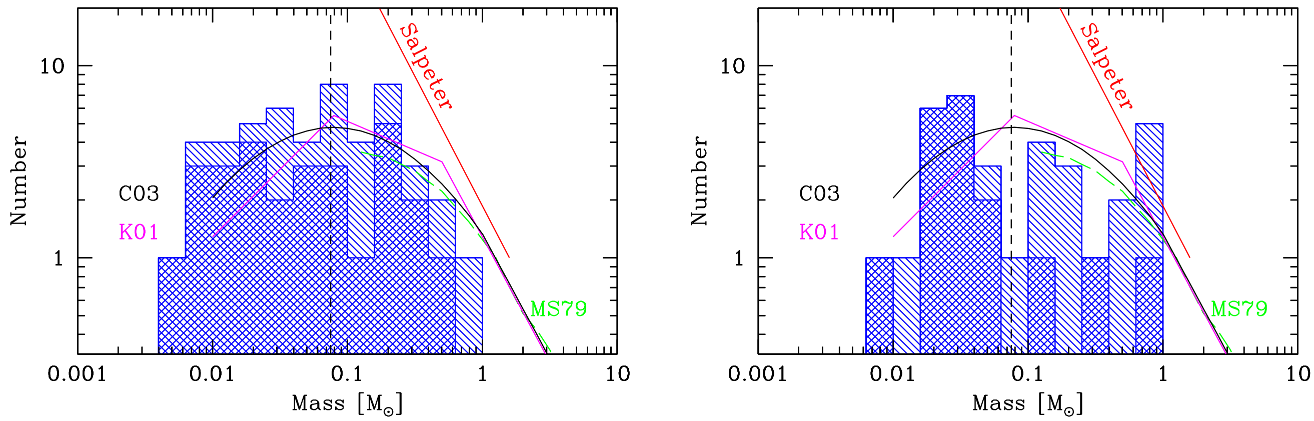

Figure 8. The initial mass functions produced by Calculations 1 and 3. Calculation 3 (righthand panel) is identical to Calculation 1 (lefthand panel), except that the collapsing gas begins heating at a lower density, resulting in a greater minimum brown dwarf mass. The single shaded regions show all of the objects, the double shaded regions show only those objects that have finished accreting. The mass resolution of the simulations is 0.0011 $M_{\odot}$ (i.e. 1.1 M_J), but no objects have masses lower than 4.9 M_J in Calculation 1 and 9.7 M_J in Calculation 3 due to the opacity limit for fragmentation. We also plot fits to the observed IMF from Miller & Scalo (1979) (dashed line), Kroupa (2001) (solid broken line), and Chabrier (2003) (solid curve). The Salpeter (1955) slope (solid straight line) is equal to that of Kroupa (2001) for $M > 0.5$ $M_{\odot}$. The vertical dashed line marks the star/brown dwarf boundary.

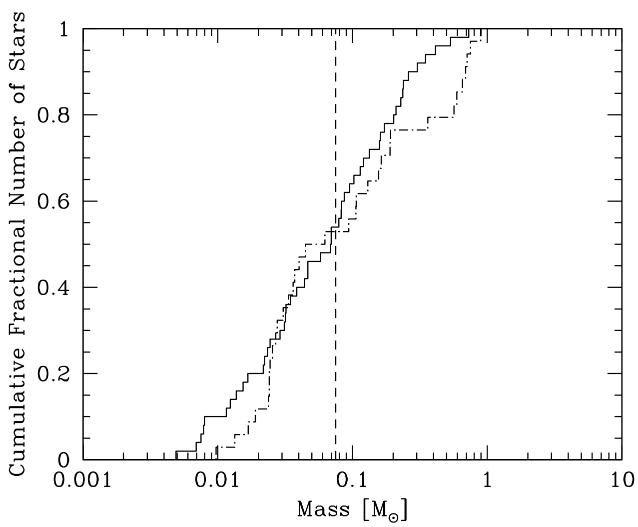

Figure 7. The *cummulative* initial mass functions produced by Calculations 1 (solid line) and 3 (dotted line). A Kolmogorov-Smirnov test on the two distributions shows that there is a 45% probability that they are drawn from the same underlying IMF (i.e., statistically, they are indistinguishable). The vertical dashed line marks the star/brown dwarf boundary.

that Goodwin, Whitworth & Ward-Thompson (2004) argue that the mass function in Taurus may different to other star-forming regions due to the fact that it only contains low-mass cores.

Observationally, in agreement with the calculations presented here, there is no evidence for brown dwarfs having a significantly higher velocity dispersion than stars (something that was suggested as a possible signature that brown dwarfs form as ejected stellar embryos by Reipurth & Clarke 2001). In fact, studies of the radial velocities of stars and brown dwarfs in the Chamaeleon I dark cloud find that brown dwarfs have a marginally lower velocity dispersion than the T Tauri stars (Joergens & Guenther 2001; Joergens 2003; Joergens 2005).

3.5 Initial mass function

A summary of the mass distributions of the stars and brown dwarfs formed in the three calculations is given in Table 1. From Calculations 1 and 2, BB2005 found that decreasing the mean thermal Jeans mass of the progenitor cloud by a factor of three resulted in a corresponding decrease in the median (characteristic) mass by a factor of almost exactly a factor of three. Thus, they concluded that the characteristic stellar mass is set by the mean thermal Jeans mass in molecular clouds. However, the opacity limit for fragmentation was the same in both these calculations, leaving open the question of its role in the origin of the IMF. We show in this section that changing the opacity limit for fragmentation only alters the value of the minimum mass cut-off and does not alter the rest of the IMF significantly.

Calculations 1 and 3 can be used to investigate the dependence of the IMF on the opacity limit for fragmentation since they are identical except for the minimum mass for fragmentation. As described in Section 2.1, the minimum mass in Calculation 3 is a factor of three greater that that in Calculation 1 (roughly 9 M_J as opposed to 3 M_J). The IMFs from the two calculations are given in Figure 8. Both calculations form roughly equal numbers of stars and brown dwarfs, indicating that changing the minimum object mass by a factor of three has little affect on the IMF (as opposed to Calculation 2 whose IMF was biased in favour of brown dwarfs). In Calculation 1, 50 objects were formed with a mean object mass of 0.118 $M_{\odot}$ and a median mass of 0.070 $M_{\odot}$. In Calculation 3, 34 objects were formed in the same time with a mean mass of 0.202 $M_{\odot}$ and a median mass of 0.054 $M_{\odot}$. As we have already discussed, heating of the gas at lower densities inhibits fragmentation, which is consistent with the fact that fewer objects are formed and their mean mass is greater. However, with such small numbers of objects, it is important to inquire whether any difference in the IMFs is statisitically significant. In Figure 7, we give the cummulative IMFs. A Kolmogorov-Smirnov test on the two distributions shows that there is a 45% probability that they are drawn from the same underlying IMF (i.e., statistically, they are indistinguishable). By contrast, BB2005 found that the IMFs from Calculations 1 and 2 had only a 1.9% probability of being drawn from the same under-

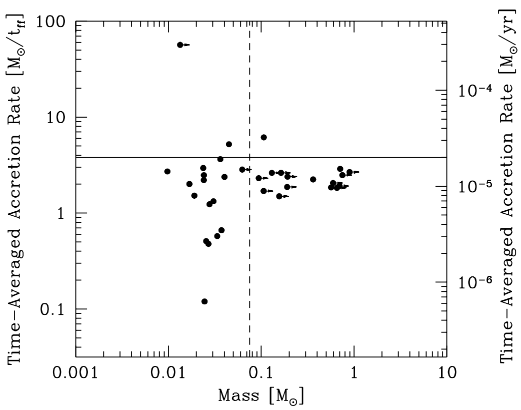

Figure 9. The time-averaged accretion rates of the objects formed in the calculation versus their final masses. The accretion rates are calculated as the final mass of an object divided by the time between their formation and the termination of their accretion or the end of the calculation. The horizontal solid line gives the arithmetic mean of the accretion rates: 1.9×10^{-5} M$_\odot$/yr. The accretion rates are given in M$_\odot$/$t_{\rm ff}$ on the left-hand axes and M$_\odot$/yr on the right-hand axes. The vertical dashed line marks the star/brown dwarf boundary.

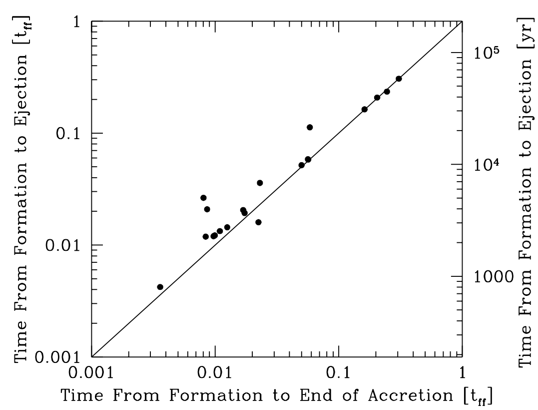

Figure 11. For each object that has stopped accreting, we plot the time between the formation of the object and its ejection from a multiple system versus the time between its formation and the termination of its accretion. As for the calculations in BB2005, these times are correlated, showing that the termination of accretion on to an object is usually associated with dynamical ejection of the object.

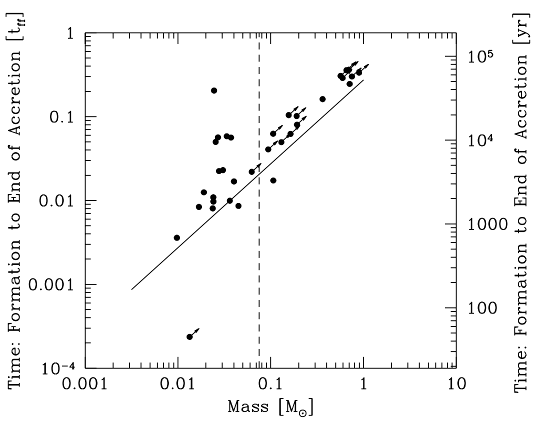

Figure 10. The time between the formation of each object and the termination of its accretion or the end of the calculation versus its final mass. As for the calculations in BB2005, there is a clear linear correlation between the time an object spends accreting and its final mass. The solid line gives the curve that the objects would lie on if each object accreted at the mean of the time-averaged accretion rates. The accretion times are given in units of the $t_{\rm ff}$ on the left-hand axes and years on the right-hand axes. The vertical dashed line marks the star/brown dwarf boundary.

lying IMF. Since the Kolmogorov-Smirnov test is most sensitive to differences in the median mass of two distributions, we conclude that the characteristic (median) mass of the IMF is quite insensitive to the value of the minimum mass which is imposed by the opacity limit for fragmentation.

Although there is no statistically significant difference in the characteristic mass from Calculations 1 and 3, the minimum object mass does increase as expected due to the change in the opacity limit for fragmentation. The lowest mass objects formed in Calculations 1 and 2 were 4.9 M$_{\rm J}$ and 2.9 M$_{\rm J}$, respectively. Thus, we assume the minimum mass for their equation of state is $\approx$ 3 M$_{\rm J}$. Calculation 3 should then have a minimum object mass of $\approx$ 9 M$_{\rm J}$. Indeed, the lowest mass brown dwarf formed has a mass of 9.7 M$_{\rm J}$.

We note that the lowest mass objects in all three calculations were ejected before the end of the calculations and none of them are still accreting. The mimimum resolvable mass in the calculations is 1.1 M$_{\rm J}$ (see Section 2.4).

In Figure 8, we compare the IMFs from Calculations 1 and 3 with parameterizations of the observed Galactic IMF by Miller & Scalo (1979), Kroupa (2001), and Chabrier (2003). Calculation 1 is in good agreement with Chabrier's single star IMF (solid curve), although we cannot yet test the form of the high-mass end of the IMF (masses $\gtrsim 1$ M$_\odot$) with calculations that simultaneously resolve down to the opacity limit for fragmentation. It is difficult to compare Calculation 3 with the parameterized IMFs due to the small number of objects formed but, within the large uncertainties, it too is consistent with the observed IMF.

BB2005 investigated in detail the origin of the IMF from Calculations 1 and 2. Since all objects in the calculations begin as opacity limited fragments at the minimum mass and then accrete to their final masses, low-mass objects could originate from objects with low accretion rates or from objects with a typical accretion rate whose accretion is terminated shortly after they form (e.g., by ejection in a dynamical interaction with other objects).

Following BB2005, in Figure 9, we plot the time-averaged accretion rates of all the objects in Calculation 3 as a function of their final masses. A time-averaged accretion rate is defined as the mass of an object at the end of the calculation divided by the time over which it accreted that mass. The accretion time is measured from the formation of an object (i.e., the insertion of a sink particle) to the *last* time at which its accretion rate drops below 10^{-7} M$_\odot$/yr, or the end of the calculation (which ever occurs first). We also define an ejection time, which is the time between the formation of an object and *last* time the magnitude of its acceleration drops below 2000 km/s/Myr (or the end of the calculation). The acceleration criterion is based on the fact that once an object is ejected from a stellar cluster through a dynamical encounter, its acceleration will drop to a low value. The specific value of the acceleration was chosen by comparing animations and graphs of acceleration versus time for individual objects. As with Calculations 1 and 2, the time-averaged accretion rates of the objects have a significant dispersion. How-

Object Numbers	M_1 $M_\odot$	M_2 $M_\odot$	q	a	e	Comments
6,8	0.75	0.59	0.79	1.0*	0.54*	
1,2	0.69	0.65	0.94	5.1*	0.77*	
24,28	0.19	0.11	0.55	5.8	0.22	
31,32	0.13	0.09	0.72	24	0.33	
5,22	0.57	0.16	0.28	39	0.54	
(24,28),29	(0.30)	0.16	0.55	40	0.22	
(31,32),23	(0.22)	0.19	0.85	186	0.27	System 1; In Core 2
3,(5,22)	0.90	(0.72)	0.81	599	0.13	
(1,2),(6,8)	(1.35)	(1.34)	1.00	217	0.37	System 2; In Core 1
(3,(5,22)),17	(1.62)	0.034	0.021	787	0.81	BD companion; System 3; In Core 1
((24,28),29),34	(0.46)	0.013	0.029	1794	0.85	BD companion (accreting); System 4; In Core 3

Table 3. The properties of the 4 multiple systems with semi-major axes less than 2000 AU formed in Calculation 3 (see also Figure 11). One of these systems is a triple while the other three are quadruple systems. The structure of each system is described using a binary hierarchy. For each 'binary' we give the masses of the primary M_1 and secondary M_2, the mass ratio $q = M_2/M_1$, the semi-major axis a, and the eccentricity e. The combined masses of multiple systems are given in parentheses. Orbital quantities marked with asterisks are unreliable because these close binaries have periastron distances less than the gravitational softening length. When the calculation is stopped, all four systems are unstable and/or are still accreting, so their final states are unknown. In the comments, BD companion refers to a wide brown dwarf companion to the tighter triple systems.

ever, there is no systematic trend for the lower-mass objects to have lower time-averaged accretion rates.

In Figure 10 we plot the time between the formation of an object and the termination of its accretion (or the end of the calculation) versus the final mass of the object. Those points with arrows denote those objects that are still accreting significantly at the end of the calculation. Accreting objects would move towards the upper right of the diagrams if the calculations were extended. Again, as with Calculations 1 and 2, it is clear that *the lower the final mass of the object, the earlier its accretion was terminated*. This is the origin of the mass distribution of the objects.

To check that the termination of the accretion is caused by the ejection of objects during dynamical interactions, in Figure 11, we plot the time between the formation of an object and its ejection from a stellar group versus the time between the formation of an object and the termination of its accretion. In this figure, we only plot those objects that have stopped accreting and reached their final masses by the end of the calculations. As in Calculations 1 and 2, the ejection and accretion times are closely correlated, showing that *the termination of accretion on to an object is usually associated with dynamical ejection of the object*. These results confirm the speculation of Reipurth & Clarke (2001) and the conclusions of Bate et al. (2002a) and BB2005 that brown dwarfs are 'failed stars'. They fall short of reaching stellar masses because they are cut off from their source of accretion prematurely due to ejection in dynamical interactions.

3.6 Multiple systems

In all three calculations, the dominant formation mechanism for binary and multiple systems was fragmentation, either of gaseous filaments (e.g. Bastein 1983; Bastien et al. 1991; Inutsuka & Miyama 1992) or of massive circumstellar discs (e.g. Bonnell 1994; Bate & Bonnell 1994; Whitworth et al. 1995; Burkert, Bate & Bodenheimer 1997; Hennebelle et al. 2004). Star-disc encounters played an important role in truncating discs (Section 3.7), and in dissipating kinetic energy (c.f. Larson 2002), but they did not play a significant role in forming binary and multiple systems from unbound objects (c.f. Clarke & Pringle 1991a). Only two star-disc encounters resulted in the formation of multiple systems in Calculation 1, while in Calculation 2 there was no obvious example of a multiple system being formed via a star-disc encounter.

In Calculation 3, there are three occurences of star-disc encounters resulting in the formation of multiple systems. Given that there are only four multiple systems at the end of the calculation (which contain 5 binaries), star-disc encounters seem to play a greater role in Calculation 3. As in Section 3.4, which discussed velocity dispersion, we can attribute the greater importance of star-disc interactions in creating multiple systems to the smaller sizes of the stellar groups in Calculation 3. As pointed out by Clarke & Pringle (1991), star-disc encounters in larger$-N$ clusters are less likely to result in capture because the virial speeds in the clusters will be higher and discs are more likely to be dispersed by high-velocity encounters prior to undergoing potential star-disc captures.

3.6.1 *Multiplicity*

When Calculation 3 was stopped, there were 19 single objects, 1 triple, and 3 quadruple systems (taking any objects with semi-major axes greater than 2000 AU to be essentially unbound). The properties of the 4 multiple systems are displayed in Table 3 and in Figure 12. Two of these systems originated in the main dense core, and one each in Cores 2 and 3. Within these systems there are five binaries (i.e., none have been ejected). The two multiple systems in Core 1 and four of the ejected brown dwarfs are still very weakly bound to each other, but are all at large distances from each other. The two multiple systems in Cores 2 and 3 are also marginally bound to each other.

Calculation 3 produces a high companion star fraction

$$CSF = \frac{B + 2T + 3Q + ...}{S + B + T + Q + ...} \quad (2)$$

of $11/23 = 48$ percent, where S is the number of single stars, B is the number of binaries, T is the number of triples, etc. Alternately, the number of companions divided by the total number of objects is $11/34 = 32$ percent. These percentages are similar to those of Calculation 1. Although the systems with more than two components will continue to evolve and some will probably eject more mem-

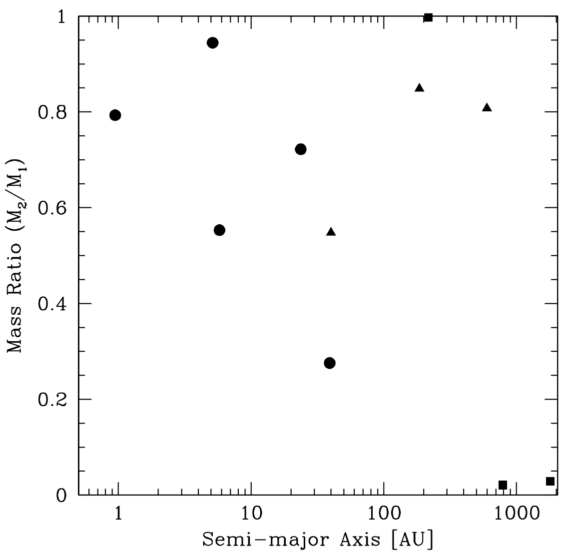

Figure 12. Mass ratios versus semi-major axes of the binary, triple and quadruple systems that exist at the end of the calculation (see also Table 3). Binaries are plotted with circles, triples with triangles and quadruple systems with squares. This figure should be compared with Figure 12 of BBB2003 and Figure 11 of BB2005 for the equivalent results from the other calculations. Calculation 1 produced no wide binaries (separations > 10 AU) and no binaries with mass ratios $M_2/M_1 \lesssim 0.3$. Calculation 2 produced five wide binaries and three binaries with mass ratios $M_2/M_1 < 0.2$. This calculation produces wide binaries (separations > 10 AU), but the lowest mass ratio is $M_2/M_1 = 0.28$.

bers, it is plausible that the final companion star frequency will be high, as required by observations of star-forming regions (Ghez, Neugebauer & Matthews 1993; Leinert et al. 1993; Richichi et al. 1994; Simon et al. 1995; Ghez et al. 1997; Duchêne 1999).

As with Calculations 1 and 2, Calculation 3 produces a realistic frequency of close binaries (separations < 10 AU) even though no two objects form closer than 13 AU from each other due to the opacity limit for fragmentation (see Bate et al. 2002b for a full discussion). Thus, although the change in the equation of state of the gas inhibits fragmentation more in Calculation 3 than in Calculation 1, this does not seem to affect the ability of close binaries to form. Even if all wider systems break up, the resulting frequency of close binaries would be $3/31 \approx 10$ percent. The corresponding values from Calculations 1 and 2 were 16 percent and 7 percent, respectively. The observed value is ≈ 20 percent (Duquennoy & Mayor 1991). However, Duquennoy & Mayor were not sensitive to brown dwarfs. If only stars are considered, the frequency of close binaries becomes $3/13 \approx 23$ percent (for Calculations 1 and 2 the corresponding frequencies were similar at $5/18 \approx 28$ percent and $4/15 \approx 27$ percent, respectively). As in Calculations 1 and 2, there is a preference for close binaries to have equal masses (all three have mass ratios of $M_2/M_1 > 0.5$), and the frequency of close binaries is higher for more massive primaries – 6 of the 16 stars are members of close binaries, while no brown dwarfs are in close binaries. These preferences result from the formation mechanisms of close systems as discussed by Bate et al. (2002b).

3.6.2 *Brown-dwarf companions to stars and brown dwarfs*

Together, Calculations 1 and 2 produced 6 binaries consisting only of very-low-mass (VLM) stars ($M < 0.09$ M$_\odot$) or brown dwarfs out of ≈ 80 VLM or brown dwarf systems, implying a frequency of binary brown dwarfs of ∼ 8 percent. Calculation 3 is consistent with this frequency in that it produced no VLM binaries from ≈ 18 VLM objects. Together, the three calculations give an overall VLM binary frequency of ≈ 6 percent. For star-brown dwarf binary systems, the frequencies are also very low. Calculation 1 one produced one binary system consisting of a star (0.13 M$_\odot$) and a brown dwarf (0.04 M$_\odot$). The system had a separation of 7 AU and was part of an unstable septuple system. Both objects were still accreting. Calculations 2 and 3 did not produce any such star/brown dwarf binary systems. The reasons for these low frequencies are discussed by BB2005.

The observed frequency of very-low-mass and brown dwarf binaries is ≈ 15 percent (Reid et al. 2001; Close et al. 2002, 2003; Bouy et al. 2003; Burgasser et al. 2003; Gizis et al. 2003; Martín et al. 2003; Siegler et al. 2005). Note, however, that the frequency of binary brown dwarfs as wide companions to stars may be higher (Burgasser, Kirkpatrick & Lowrance 2005). The vast majority of binary brown dwarfs have separations less than 20 AU (Close et al. 2003; Siegler et al. 2005), but there is at least one binary brown dwarf system with a separation greater than 200 AU (Luhman 2004a). Thus, the calculations correctly favour the production of close binary brown dwarfs, but they under-produce binary brown dwarfs by roughly a factor of two. This difficulty may be associated with our resolution limits – we are unable to resolve circumstellar discs at radii $\lesssim 10$ AU, and gravitational interactions between stars/brown dwarfs are softened at separations less than 4 AU. The rarity of brown dwarfs orbiting stars is consistent both with the so called brown dwarf desert discovered through Doppler searches for planets orbiting solar-type stars (Marcy & Butler 2000) and from imaging surveys for wide systems (Gizis et al. 2001).

Finally, many of the multiple systems in all of our calculations have wide brown dwarf companions. Although they are still dynamically evolving when the calculations are stopped, we note that the small-scale turbulent star-formation simulations of Delgado-Donate et al. (2004), which were evolved until the systems reached dynamical stability, also predict that many close stellar binary systems should have wide brown dwarf companions.

3.7 Protoplanetary discs

The calculations resolve gaseous discs with radii $\gtrsim 10$ AU around the young stars and brown dwarfs. Discs with typical radii of ∼ 50 AU form around many of the objects due to the infall of gas with high specific angular momentum. However, in all calculations discs are severely truncated in subsequent dynamical interactions, leaving most of them too small to form analogues of our solar system (see BBB2003). The six resolved discs at the end of Calculation 3 are listed in Table 4, and in Figure 13 we plot the closest encounter distance for each object during the calculation as a function of its final mass. All but two stars have had encounters closer than 10 AU. None of the brown dwarfs or ejected stars have resolved discs and the stars with resolved discs are all members of multiple systems. Although they have had very close encounters, subsequent infalling gas has build up circumbinary and circumtriple discs around them. This is a feature of all three calculations.

Disc Radius AU	Encircled Objects	Comments
300	(31,32),23	Circumtriple disc (Figure 2, $t = 1.40t_{\rm ff}$, right)
130	(24,28),29	Circumtriple disc (Figure 4, $t = 1.40t_{\rm ff}$)
120	5,22	Circumbinary disc, forms triple system with 3
110	3	Forms triple system with 5,22 (Figure 2, $t = 1.40t_{\rm ff}$, left)
70	6,8	Circumbinary disc, forms quadruple system with 1,2
60	1,2	Circumbinary disc, forms quadruple system with 6,8

Table 4. The discs that exist around objects when the calculation is stopped. Discs with radii $\lesssim$ 10 AU are not resolved. Unlike Calculation 1, in Calculation 3 no objects are ejected with resolved discs. This table should be compared with Tables 4 of BBB2003 and BB2005 for the equivalent results from Calculations 1 and 2, respectively.

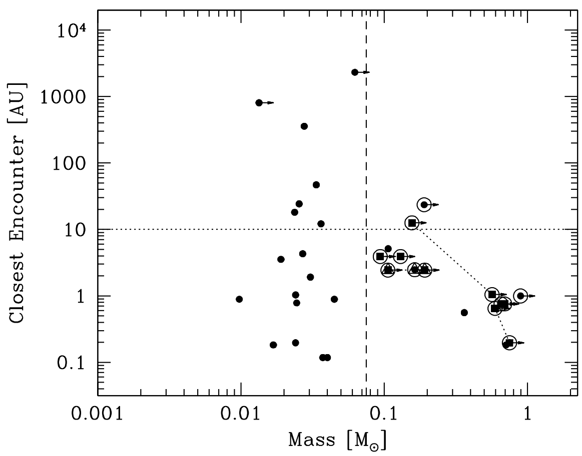

Figure 13. The closest encounter distance of each star or brown dwarf during the calculation versus the object's final mass. This figure should be compared with Figure 14 of BBB2003 and Figure 12 of BB2005 for the equivalent results from Calculations 1 and 2. Objects that are still accreting significantly at the end of the calculation are denoted with arrows indicating that they are still evolving and that their masses are lower limits. Objects that have resolved discs at the end of the simulation are circled. Discs smaller than $\approx$ 10 AU (horizontal dotted line) cannot be resolved by the simulation. Objects that have had close encounters may still have resolved discs due to subsequent accretion from the cloud. Note that there are only 6 resolved discs at the end of the simulation, but many surround binary and higher-order multiple systems (hence the 13 circles in the figure). Binaries (semi-major axes < 100 AU) are plotted with the two components connected by dotted lines and squares are used as opposed to circles. Components of triple systems whose orbits have semi-major axes $10 < a < 100$ AU are denoted by triangles. All of the binaries are surrounded by resolved discs. Encounter distances less than 4 AU are upper limits since the point mass potential is softened within this radius. The vertical dashed line marks the star/brown dwarf boundary. The two brown dwarfs in the top left corner of the figure that are still accreting formed shortly before the calculation was stopped are thus still evolving rapidly. They may not end up as brown dwarfs. There are no brown dwarfs that have resolved discs and have finished accreting.

4 DISCUSSION

4.1 The accretion/ejection model for the IMF

BB2005 argued that the IMFs produced by Calculations 1 and 2 originated from a combination of accretion and dynamical ejections which terminate the accretion. As shown in Section 3.5, their conclusions are supported by Calculation 3. They proposed a very simple model for the origin of the IMF and found that it reproduced the IMFs obtained from the first two calculations very well. Here we show that the model also produces an acceptable fit to the IMF from Calculation 3.

The simple accretion/ejection model for the IMF produced by a star-forming molecular cloud is as follows.

- We assume all objects begin with masses set by the opacity limit for fragmentation (3 M_J for Calculations 1 and 2 and 9 M_J for Calculation 3) and then accrete at a fixed rate $\dot{M}$ until they are ejected.
- We assume the accretion rates of individual objects are drawn from a log-normal distribution with a mean accretion rate (in log-space) given by $\log_{10}(\overline{\dot{M}}) = \overline{\log_{10}(\dot{M})}$ and a dispersion of σ dex (i.e. $\log_{10}(\dot{M}) = \log_{10}(\overline{\dot{M}}) + \sigma G$, where G is a random Gaussian deviate with zero mean and unity variance).
- The ejection of protostars from an N-body system is a stochastic process that can be described in terms of the half-life of the process. We assume that there is a single parameter, $\tau_{\rm eject}$, that is the characteristic timescale between the formation of an object and its ejection from the cloud. The probability of an individual object being ejected is then $\exp(-t/\tau_{\rm eject})$ where t is the time elapsed since its formation.

Calculation 3 supports this model in that Figure 9 shows there is no correlation between an object's time-averaged accretion rate and its final mass, while Figure 10 shows a strong correlation between the time an object spends accreting and its final mass and Figure 11 shows that accretion is usually terminated by gravitational interactions with other objects leading to dynamical ejection.

Assuming that the cloud forms a large number of objects, N, and that the time it evolves for is much greater than the characteristic ejection time, $T \gg \tau_{\rm eject}$, then a semi-analytic formula can be derived for the form of the IMF (BB2005) and there are essentially only three free parameters in the model. These are the mean accretion rate times the ejection timescale, $\overline{M} = \overline{\dot{M}}\tau_{\rm eject}$, the dispersion in the time-averaged accretion rates, σ, and the minimum mass provided by the opacity limit for fragmentation, $M_{\rm min}$. If $\overline{M} >> M_{\rm min}$, $\overline{M}$ is the characteristic mass of an object.

4.1.1 *Reproduction of the hydrodynamical IMF*

The hydrodynamical calculations are not followed until all the stars and brown dwarfs have finished accreting (i.e., the IMF is not fully formed). It is not the case that $T \gg \tau_{\rm eject}$. This must be taken into account when calculating simple accretion/ejection models for comparison with the IMFs from the hydrodynamical calculations. To do this, we evolved the simple models over the same periods

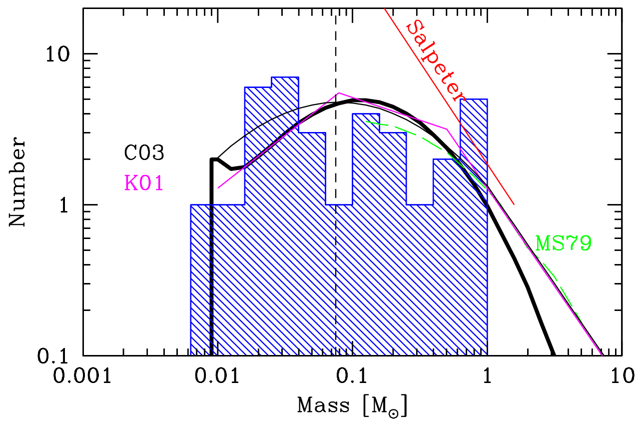

Figure 14. The initial mass functions produced by Calculation 3 (histogram) and its fit using the simple accretion/ejection IMF model (thick solid line). Statistically, the hydrodynamical and the model IMFs are indistinguishable. Also shown are the Salpeter slope (solid straight line), and the Miller & Scalo (1979) (dashed line), Kroupa (2001) (solid broken line) and Chabrier (2003) mass functions. The vertical dashed line is the stellar-substellar boundary.

Model	$M_{\rm min}$ M$_\odot$	$\bar{\dot{M}}$ M$_\odot$/yr	σ Dex.	$\tau_{\rm eject}$ yr	T yr
1	0.003	6.17×10^{-6}	0.33	3.2×10^{4}	6.91×10^{4}
2	0.003	7.18×10^{-6}	0.50	9.3×10^{3}	3.67×10^{4}
3	0.009	1.00×10^{-5}	0.41	2.5×10^{4}	6.91×10^{4}

Table 5. The parameters of the simple accretion/ejection IMF models that should reproduce the IMFs from the three hydrodynamical calculations (Figure 14). There are essentially three parameters in the models, the mean accretion rate times the characteristic timescale for ejection ($\bar{\dot{M}}\tau_{\rm eject}$), the dispersion in the accretion rates σ, and the minimum mass set by the opacity limit for fragmentation $M_{\rm min}$. The time period over which the simulations are run, T, has a small effect on the form of the IMF. For example, the peak in the model IMF (Figure 14) at very low masses is because one object formed shortly before the calculation was stopped and therefore this object does not usually manage to accrete much mass in the model.

of time, T, that the hydrodynamical simulations took to form their stars and brown dwarfs and take the times of formation of each of the objects directly from the hydrodynamical simulations (i.e., from Figure 5 for Calculation 3).

We generated a model IMF for comparison with the IMF from Calculation 3. The model IMF is the average of 30000 random realisations of the simple accretion/ejection model, keeping the values of the input parameters fixed. The parameter values are given in Table 5. It is important to note that these parameters were *not* varied in order to obtain good fits to the hydrodynamical IMF. Rather, *the values of the parameters were taken directly from the hydrodynamical simulation*. There is no freedom to vary the parameters in order to obtain a better fit. The mean accretion rate of the objects, $\bar{\dot{M}}$, and the dispersion in the accretion rates, σ, were set equal to the mean (in log-space) of the time-averaged accretion rates and their dispersion from Figure 9. The characteristic ejection times, $\tau_{\rm eject}$, were set so that the mean numbers of objects ejected from the 30000 random realisations matched the number of objects ejected during each of the hydrodynamical calculations (19 for Calculation 3).

Figure 14 shows that the simple accretion/ejection model matches the hydrodynamical IMF reasonably well. A Kolmogorov-Smirnov test gives a 6.6 percent probability that the hydrodynamical IMF could have been drawn from the model IMF (i.e., they are consistent with each other). For Calculations 1 and 2, the hydrodynamical IMFs have 92 and 27 percent probabilities of being drawn from the simple accretion/ejection model IMFs, respectively (see BB2005).

4.2 The dependence of the IMF on temperature

Since the three hydrodynamical calculations discussed in this paper are very time consuming, they have been carefully designed to enable the origins of the statistical properties of stars to be investigated in the most possible detail. Comparison of Calculations 1 and 2 allowed BB2005 to investigate the dependence of star formation on the mean density $\bar{\rho}$ of the molecular cloud and, therefore, the mean thermal Jeans mass which scales as $1/\sqrt{\rho}$. Comparison of Calculations 1 and 3 allows the role of the opacity limit for fragmentation to be investigated. However, it is also possible to compare Calculations 2 with Calculations 1 and 3 to investigate the dependence of star formation on the *temperature* of a molecular cloud and, thus, test further BB2005's assertion that the characteristic stellar mass depends primarily on the mean thermal Jeans mass of a star-forming molecular cloud.

Purely isothermal models of the collapse of molecular clouds are often said to be scale-free in that they can be rescaled arbitrarily to different model clouds with different masses or radii. In these cases, only dimensionless quantities such as the ratio of thermal to gravitational potential energies remain fixed.

The calculations discussed in this paper have a characteristic density introduced through the change in the equation of state that occurs at the critical density $\rho_{\rm crit}$. However, they can still be rescaled. Calculation 2 differed to Calculation 1 in that its density was greater by a factor of nine, decreasing the mean thermal Jeans mass from 1 M$_\odot$ in Calculation 1 to 1/3 M$_\odot$. This was achieved by decreasing the radius by a factor of $9^{1/3} \approx 2.08$. The only other difference was that, because the initial 'turbulence' was normalised so that the kinetic energy equaled the magnitude of the gravitational potential energy while the initial temperature was kept at 10 K, the Mach number was larger in Calculation 2 by a factor of $9^{1/6} \approx 1.44$.

We can also inquire what the star formation would be like if Calculation 2 was re-run, but with a greater initial cloud temperature. In particular, if we increased the temperature by a factor of $3^{2/3} = 2.08$, this would give the same initial mean thermal Jeans mass of 1 M$_\odot$ as that in Calculations 1 and 3. Thus, *rescaling* the results of Calculations 1 and 3 by reducing all distances by a factor 2.08 gives the same evolution as running Calculation 2 with an initial temperature of 20.8 K instead of 10 K. The initial densities, velocities, and free-fall times of the clouds are the same as they were in Calculation 2. But now the results give the properties of stars formed in hotter clouds with critical densities of $\rho_{\rm crit} = 9.0 \times 10^{-13}$ and 1.0×10^{-13} for Calculations 1 and 3, respectively. The only slight difference between these rescaled versions of Calculations 1 and 3 and performing entirely new calculations of hotter clouds with these critical densities is that Calculations 1, 2, and 3 all used sink particles to model the stars and brown dwarfs with accretion radii of 5 AU and gravitational softening of dynamical interactions within 4 AU. The rescaled versions of Calculations 1 and 3 have sink particle radii and gravitational softening 2.08 times smaller than these values. However, the whole assumption of using sink particles is that the results are not sensitive to their introduction.

Certainly, it is assumed that the results do not change dramatically by varying accretion radii by factors of two.

With this one caveat, we can use the rescaled results to investigate the dependence of star formation on the temperature of a molecular cloud. Changing the distance scale of Calculations 1 and 3 does not alter the mass scaling. Thus, the IMFs of Calculations 1 and 3 do not change due to the rescaling. BB2005 showed that the characteristic (median) mass of Calculation 2 is a factor of 3.04 smaller than that of Calculation 1, following almost exactly the change in the mean thermal Jeans mass. Thus, the characteristic (median) mass of the rescaled Calculation 1 (which models a cloud identical to that of Calculation 2 except that its temperature is 2.08 times hotter) also follows the increase in the mean thermal Jeans mass of the cloud due to the increase in the temperature T (the Jeans mass scales as $T^{3/2}$). Furthermore, since the IMFs of Calculations 1 and 3 are indistinguishable (Section 8), the opacity limit for fragmentation which is modelled by the critical density at which the equation of state changes also plays no significant role in determining the IMF in the hotter high-density clouds represented by the rescaled versions of Calculations 1 and 3.

In summary, the characteristic (median) mass of the IMF is set by the mean thermal Jeans mass in the progenitor cloud (determined by the density and temperature), and not by the opacity limit for fragmentation (determined by metallicity). The question then arises as to what sets the mean thermal Jeans mass in a molecular cloud. Larson (2005) has argued that this is set by a change in the thermal behaviour of the gas forming molecular clouds when the cooling switches from being dominated by line cooling to dust cooling. This has been backed up by hydrodynamical simulations that study how the characteristic mass of fragments depends on the equation of state at low densities (Jappsen et al. 2005). Therefore, it is important to note that although metallicity may not affect the IMF above the low-mass cut-off through its effect on the opacity limit for fragmentation, it may still have an affect on the characteristic mass of the IMF if it alters the cooling during molecular cloud formation and, hence, the mean thermal Jeans mass of the molecular cloud.

5 CONCLUSIONS

We have presented results from the third hydrodynamical calculation to follow the collapse of a turbulent molecular cloud to form a stellar cluster while resolving fragmentation down to the opacity limit. We compare the results with those obtained from the calculations published by Bate et al. (2002a,2002b,2003) and Bate & Bonnell (2005). The new calculation is identical to that of Bate et al. (2003), except for the density above which the opacity limit inhibits fragmentation. It can also be rescaled to model a cloud that is identical to that of Bate & Bonnell (2005) except that the initial gas has a temperature of 20.8 K instead of 10 K.

We find that although the minimum mass of a brown dwarf increases when the opacity limit for fragmentation sets in at a lower gas density (i.e., a lower metallicity), the form of the IMF above the minimum cut-off mass is independent of the opacity limit for fragmentation.

Rather than being set by the opacity limit for fragmentation, Bate & Bonnell (2005) showed that the characteristic (median) mass of the IMF varies linearly with the mean thermal Jeans mass in the molecular cloud. They did this by running two calculations with different densities. However, the mean thermal Jeans mass is a function of both density and temperature. Here we also confirm that the characteristic mass of the IMF varies linearly with the mean thermal Jeans mass by comparing two clouds with the same initial densities, but with different initial temperatures.

Finally, the new calculation discussed in this paper displays several differences from the earlier calculations. Because collapsing gas begins to heat at a lower density, the degree of fragmentation is reduced and the stellar groups contain fewer objects. This has two main effects. First, the velocity dispersion of multiple stars is lower than that of single objects because it is difficult to eject binaries from small−N groups (Section 3.4). Second, star-disc interactions play a greater role in forming binary and multiple systems than in the earlier calculations because the velocity dispersions of the objects in smaller groups tend to be lower and discs undergo fewer dispersive encounters (Section 3.6). We also note that Goodwin et al. (2004) found that the somewhat peculiar IMF of Taurus (with a peak at ≈ 0.8 M$_\odot$ IMF and few low-mass objects; Briceño et al. 2002; Luhman 2004b) may result from the molecular cloud being composed of a collection of low-mass cores with similar masses. Together, these results imply that in a region like Taurus, which contains only low-mass cores forming small groups of stars, the IMF may be abnormal, multiple systems may have a smaller velocity dispersion than singles, and star-disc encounters may be more important for forming multiple systems than in larger star clusters, which might help explain why binaries seem abnormally abundant in Taurus (Leinert et al. 2003; Ghez et al. 2003; Duchêne 1999).

ACKNOWLEDGMENTS

The computations reported here were performed using the U.K. Astrophysical Fluids Facility (UKAFF). MRB is grateful for the support of a Philip Leverhulme Prize.

REFERENCES

Bastien P., 1983, A&A, 119, 109
Bastien P., Arcoragi J., Benz W., Bonnell I., Martel H., 1991, ApJ, 378, 255
Bate M. R., Bonnell I. A., 2005, MNRAS, 356, 1201
Bate M. R., Bonnell I. A., Bromm V., 2002a, MNRAS, 332, L65
Bate M. R., Bonnell I. A., Bromm V., 2002b, MNRAS, 336, 705
Bate M. R., Bonnell I. A., Bromm V., 2003, MNRAS, 339, 577
Bate M. R., Bonnell I. A., Price N. M., 1995, MNRAS, 277, 362
Bate M. R., Burkert A., 1997, MNRAS, 288, 1060
Benz W., 1990, in Buchler J. R., ed., The Numerical Modeling of Nonlinear Stellar Pulsations: Problems and Prospects. Kluwer, Dordrecht, p. 269
Benz W., Bowers R. L., Cameron A. G. W., Press W., 1990, ApJ, 348, 647
Bonnell I. A., 1994, MNRAS, 269, 837
Bonnell I. A., Bate M. R., 1994, MNRAS, 271, 999
Boss A. P., Fisher R. T., Klein R. I., McKee C. F., 2000, ApJ, 528, 325
Bouy H., Brandner W., Martín E. L., Delfosse X., Allard F., Basri, G., 2003, AJ, 126, 1526
Briceño C., Luhman K. L., Hartmann L., Stauffer J. R., Kirkpatrick J. D., 2002, ApJ, 580, 317
Burgasser A. J., Kirkpatrick J. D., Lowrance P. J., 2005, astro-ph/0503379
Burgasser A. J., Kirkpatrick J. D., Reid I. N., Brown M. E., Miskey C. L., Gizis J. E., 2003, ApJ, 586, 512
Burkert A., Bate, M. R., Bodenheimer P., 1997, MNRAS, 289, 497
Chabrier G., 2003, PASP, 115, 763
Clarke C. J., Pringle J. E., 1991, MNRAS, 249, 584
Close L. M., Siegler N., Freed M., Biller B., 2003, ApJ, 587, 407
Close L. M., Siegler N., Potter D., Brandner W., Liebert J., 2002, ApJ, 567, L53
Delgado-Donate E. J., Clarke C. J., Bate M. R., 2003, MNRAS, 342, 926

Delgado-Donate E. J., Clarke C. J., Bate M. R., Hodgkin S. T., 2004, MNRAS, 351, 617
Duchˆene G., 1999, A&A, 341, 547
Duquennoy A., Mayor M., 1991, A&A, 248, 485
Elmegreen B. G., 2000, ApJ, 530, 277
Ghez A. M., Neugebauer G., Matthews K., 1993, AJ, 106, 2005
Ghez A. M., McCarthy D. W., Patience J. L., Beck T. L., 1997, ApJ, 481, 378
Gizis J. E., Kirkpatrick J. D., Burgasser A., Reid I. N., Monet D. G., Liebert J., Wilson J. C., 2001, ApJ, 551, L163
Gizis J. E., Reid I. N., Knapp G. R., Liebert J., Kirkpatrick J. D., Koerner D. W., Burgasser A. J., 2003, AJ, 125, 3302
Goodwin S. P., Whitworth A. P., Ward-Thompson D., 2004, A&A, 419, 543
Hartmann L., Ballesteros-Paredes J., Bergin E. A., 2001, ApJ, 562, 852
Hennebelle P., Whitworth A. P., Cha S.-H., Goodwin S. P., 2004, MNRAS, 348, 687
Hoyle F., 1953, ApJ, 118, 513
Inutsuka S., Miyama S. M., 1992, ApJ, 388, 392
Jappsen A.-K., Klessen R. S., Larson R. B., Li Y., Mac Low M. M., astro-ph/0410351
Joergens V., 2003, PhD thesis, Ludwigs-Maximilians Universität München
Joergens V., 2005, Rev. Mod. Astron., 18, in press
Joergens V., Guenther E., 2001, A&A, 379, L9
Klessen R. S., 2001, ApJ, 556, 837
Klessen R. S., Burkert A., 2000, ApJS, 128, 287
Klessen R. S., Burkert A., 2001, ApJ, 549, 386
Klessen R. S., Burkert A., Bate M. R., 1998, ApJ, 501, L205,
Kroupa P., 2001, MNRAS, 322, 231
Lada E. A., 1992, ApJ, 393, L25
Larson R. B., 1992, MNRAS, 256, 641
Larson R. B., 2002, MNRAS, 332, 155
Larson R. B., 2005, MNRAS, in press
Leinert C., Zinnecker H., Weitzel N., Christou J., Ridgway S. T., Jameson R., Haas M., Lenzen R., 1993, A&A, 278, 129
Li, P. S., Norman M. L., Mac Low M., Heitsch F., 2004, ApJ, 605, 800
Low C., Lynden-Bell D., 1976, MNRAS, 176, 367
Luhman K. L., 2004a, 614, 398
Luhman K. L., 2004b, 617, 1216
Luhman K. L., Briceño C., Stauffer J. R., Hartmann L., Barrado y Navascués D., Caldwell N., 2003, ApJ, 590, 348
MacLow M. M., Klessen R. S., Burkert A., Smith M. D., Kessel O., 1998, Phys. Rev. Lett., 80, 2754
Marcy G. W., Butler R. P., 2000, PASP, 112, 137
Martín E. L., Barrado y Navascués D., Baraffe I., Bouy H., Dahm S., 2003, ApJ, 594, 525
Masunaga H., Inutsuka S., 1999, ApJ, 510, 822
Miller G. E., Scalo J. M., 1979, ApJS, 41, 513
Monaghan J. J., 1992, ARA&A, 30, 543
Monaghan J. J., Gingold R. A., 1983, J. Comput. Phys., 52, 374
Nelson A. F., 2005, MNRAS, in press.
Ostriker E. C., Stone J. M., Gammie C. F., 2001, ApJ, 546, 980
Pringle J. E., 1989, MNRAS, 239, 361
Rees M. J., 1976, MNRAS, 176, 483
Reid I. N., Gizis J. E., Kirkpatrick J. D., Koerner D. W., 2001, AJ, 121, 489
Reipurth B., Clarke, C., 2001, AJ, 122, 432
Richichi A., Leinert C., Jameson R., Zinnecker H., 1994, A&A, 287, 145
Salpeter E. E., 1955, ApJ, 121, 161
Siegler N., Close L. M., Cruz K. L., Martín E. L., Reid I. N., 2005, ApJ, 621, 1023
Silk J., 1977a, ApJ, 214, 152
Silk J., 1977b, ApJ, 214, 718
Silk J., 1995, ApJ, 438, L41
Simon M., Ghez A. M., Leinert Ch., Cassar L., Chen W. P., Howell R. R., Jameson R. F., Matthews K., Neugebauer G., Richichi A., 1995, ApJ, 443, 625
Sterzik M F., Durisen R. H., 1998, A&A, 339, 95
Truelove J. K., Klein R. I., McKee C. F., Holliman J. H., Howell L. H., Greenough J. A., 1997, ApJ, 489, L179
Whitworth A. P., 1998, MNRAS, 296, 442
Whitworth A. P., Chapman S. J., Bhattal A. S., Disney M. J., Pongracic H., Turner J. A., 1995, MNRAS, 277, 727
Wilking B. A., Lada C. J., 1983, ApJ, 274, 698